



Microwave and Hard X-Ray Observations of the 2017 September 10 Solar Limb Flare

Dale E. Gary¹, Bin Chen¹, Brian R. Dennis², Gregory D. Fleishman¹, Gordon J. Hurford³, Säm Krucker^{3,4},
James M. McTiernan³, Gelu M. Nita¹, Albert Y. Shih², Stephen M. White⁵, and Sijie Yu¹

¹ Center for Solar-Terrestrial Research, New Jersey Institute of Technology, 323 M L King Jr Boulevard, Newark, NJ 07102-1982, USA; dgary@njit.edu

² Solar Physics Laboratory, NASA Goddard Space Flight Center, Greenbelt, MD 20771, USA

³ Space Sciences Laboratory, University of California, Berkeley, CA 94720, USA

⁴ Institute for Data Science, University of Applied Sciences and Arts Northwestern Switzerland, 5210 Windisch, Switzerland

⁵ Space Vehicles Directorate, Air Force Research Laboratory, USA

Received 2018 May 11; revised 2018 June 23; accepted 2018 July 1; published 2018 August 13

Abstract

We report the first science results from the newly completed Expanded Owens Valley Solar Array (EOVSA), which obtained excellent microwave (MW) imaging spectroscopy observations of SOL2017-09-10, a classic partially occulted solar limb flare associated with an erupting flux rope. This event is also well-covered by the *Reuven Ramaty High Energy Solar Spectroscopic Imager (RHESSI)* in hard X-rays (HXRs). We present an overview of this event focusing on MW and HXR data, both associated with high-energy nonthermal electrons, and we discuss them within the context of the flare geometry and evolution revealed by extreme ultraviolet observations from the Atmospheric Imaging Assembly (AIA) aboard the *Solar Dynamics Observatory*. The EOVSA and *RHESSI* data reveal the evolving spatial and energy distribution of high-energy electrons throughout the entire flaring region. The results suggest that the MW and HXR sources largely arise from a common nonthermal electron population, although the MW imaging spectroscopy provides information over a much larger volume of the corona.

Key words: Sun: flares – Sun: radio radiation – Sun: X-rays, gamma rays

1. Introduction

It has long been recognized that microwave (MW) and hard X-ray (HXR) observations of solar flares are highly complementary, both emissions arising from high-energy electrons accelerated during the energy release process. Although these two emissions often have extremely similar light curves during the impulsive phase (Dennis 1988), important differences remain, namely that the MW-producing gyrosynchrotron emission arises mainly from a trapped population of electrons spiraling in coronal magnetic loops, while the HXR emission is dominated by bremsstrahlung from precipitating electrons escaping to the footpoints of those same loops. HXR images and spectra often tell a more complex story, however, revealing both a super-hot thermal component in the corona and sometimes, especially in cases of occulted or partially occulted limb flares, a nonthermal “above-the-looptop” coronal source (e.g., Masuda et al. 1994; Krucker & Lin 2008).

For more than two decades, MW studies of solar flares have been dominated by data from the solar-dedicated Nobeyama Radioheliograph (NoRH; Nakajima et al. 1994) taken at two fixed frequencies, 17 and 34 GHz. NoRH was designed to operate at optically thin frequencies well above the typically 5–10 GHz peak of the MW spectrum (Guidice & Castelli 1975; Nita et al. 2004), where the interpretation of the emission is expected to be relatively simple. The MW emission at these high frequencies comes mainly from regions of high magnetic field strengths, and hence are likely to be relatively small, compact loops, or the footpoints of larger loops (e.g., Hanaoka 1997; Nishio et al. 1997). However, large looptop sources due to efficient trapping of the nonthermal electrons have been reported (e.g., Melnikov et al. 2002). Observations by the Owens Valley Solar Array (OVSA; Wang et al. 1994), and occasionally by the Very

Large Array (e.g., Schmahl et al. 1990), revealed a richer range of phenomena that could be exploited with MW imaging spectroscopy—the use of data with simultaneous high spatial, spectral, and temporal resolution over a broad frequency range. In particular, they revealed evidence for extremely large MW sources at lower frequencies (Kucera et al. 1994; Lee et al. 1994; Fleishman et al. 2017; Kuroda et al. 2018), where emission from energetic electrons in regions of weak magnetic field becomes visible, as well as purely thermal MW sources (Gary & Hurford 1989; Fleishman et al. 2015; Wang et al. 2017).

Recognizing the potential for MW imaging spectroscopy, a concept for a new solar-dedicated array (the Frequency-Agile Solar Radiotelescope, or FASR; Gary & Keller 2004; Bastian & Gary 2005) was developed to provide the capabilities needed to exploit this technique. Although FASR has not yet been realized, its design concepts have been applied in the creation of a smaller, demonstrator array called the Expanded OVSA (EOVSA) that has been fully operational since 2017 April. This paper describes the first example of MW imaging spectroscopy from EOVSA and demonstrates that it has achieved the performance expected from earlier simulations (Gary et al. 2013). We choose for this first report an extremely well observed, partially occulted limb flare associated with an erupting flux rope, seen in profile in extreme ultraviolet (EUV) and HXR emissions. This unique combination of data fully captures the event within the framework of the standard solar flare model, also known as the CSHKP model (Carmichael 1964; Sturrock 1966; Hirayama 1974; Kopp & Pneuman 1976), but in addition, with the unprecedented MW spectral imaging, reveals new information about the extent of highly energetic (100s of keV to MeV) electrons within that framework that has heretofore been hidden.

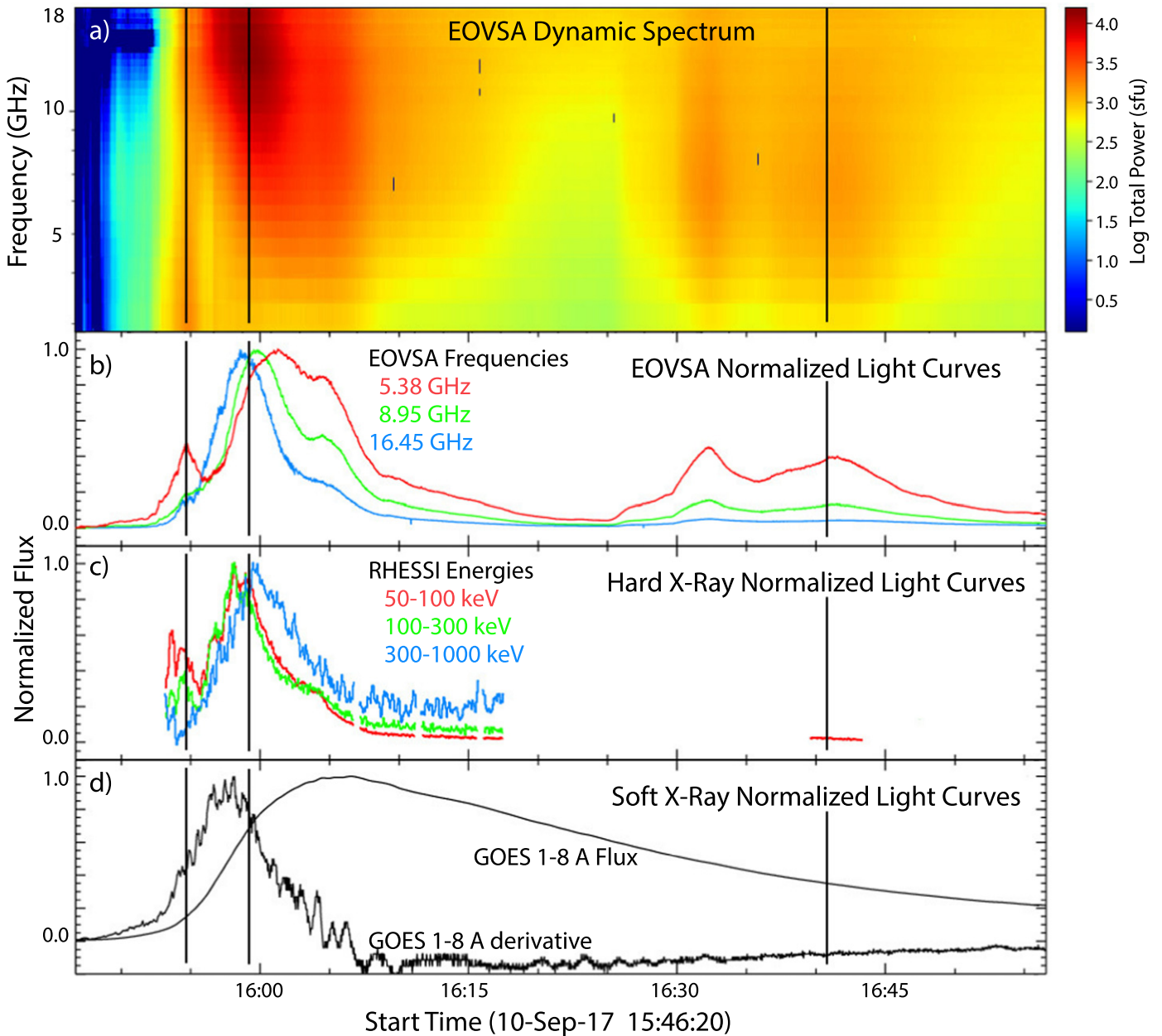


Figure 1. Dynamic MW spectrum and normalized light curves of the first ~ 1 hr of the event at different wavelengths. (a) The EOVSA total power dynamic spectrum from 2.5 to 18 GHz, with colors representing the flux density in sfu, as shown in the color bar to the right. (b) Normalized time profiles of the MW emission at three frequencies. (c) Normalized time profiles of *RHESSI* HXR counts, with a gap due to passage of the spacecraft through the South Atlantic Anomaly. (d) Normalized *GOES* 1–8 Å flux and time derivative. The vertical lines mark three times discussed in greater detail in the text.

2. Observations

We present EOVSA observations of the X8.2 flare, SOL2017-09-10, that was partially occulted by the west limb and peaked at around 16:00 UT. It continued to produce emissions in MW, EUV, X-rays, and γ -rays for many hours. The event was well observed in MW by EOVSA, in EUV by the Atmospheric Imaging Assembly (AIA; Lemen et al. 2012) on the *Solar Dynamics Observatory*, in HXR by the *Reuven Ramaty High-Energy Solar Spectroscopic Imager* (*RHESSI*; Lin et al. 2002) and the Fermi Gamma-ray Burst Monitor (Meegan et al. 2009), and in γ -rays by the *Fermi* Large Area Telescope (Atwood et al. 2009). The event has received considerable attention in the literature in the few months since

it occurred (e.g., Doschek et al. 2018; Li et al. 2018; Long et al. 2018; Omodei et al. 2018; Warren et al. 2018; Yan et al. 2018).

Figure 1 shows an overview of spatially integrated light curves for emission at different wavelengths and the total power MW dynamic spectrum from EOVSA. The light curves are normalized to unity to emphasize the differing peak times. The vertical black lines mark three specific times in the event that we focus on: (1) an early impulsive peak near 15:54 UT (t_1) that has a nearly flat MW spectrum, (2) the peak time near 16:00 UT (t_2) that has a steeply rising MW spectrum, and (3) a time near 16:41 UT (t_3), when *RHESSI* resumed solar observations after passage through the South Atlantic Anomaly (SAA). Of particular interest is the comparison of peak times. The *GOES* 1–8 Å flux derivative in Figure 1(d) peaks around

15:57 UT, close to the time of the *RHESSI* 50–300 keV light curves at 15:58 UT (Figure 1(c)). However, the peak in the higher-energy 300–1000 keV *RHESSI* light curve is delayed to 16:00 UT. This implies a progressive increase in energy of the accelerated particles during this phase of the event. For a static source, such an evolution of particle energy would be expected to shift the MW peak frequency to higher frequencies, leading to higher frequencies peaking later (e.g., Dulk 1985). However, as shown in Figure 1(b), the delay in peak time is opposite to this expectation, with higher frequencies peaking earlier (15:58:50 UT at 18 GHz) and lower frequencies peaking later (16:01:30 UT at 5.4 GHz). As the MW images will show, this progressive delay with frequency is due to a relatively slow evolution of the entire MW-emitting source region from low coronal heights with higher magnetic field strength toward greater heights and lower magnetic field strength. This spatial evolution thus leads to a more complicated total power (spatially integrated) spectral evolution, in this case actually inverting the expected delay with frequency.

As described in Gary et al. (2018, see also Nita et al. 2016), EOVSAs are designed to observe at hundreds of frequency channels spread over 34 spectral windows (spws) of 500 MHz bandwidth over the 1–18 GHz frequency range, covering the entire spectrum in 1 s. At the time of these observations, for reasons discussed in that paper, a high-pass filter was in place on each antenna to limit the observations to 2.5–18 GHz in 134 frequencies spread over 31 spws, with the width of each window limited to 160 MHz. The lowest spw is as yet uncalibrated, leaving 30 usable spws. For simplicity in this first-results paper, we combine the frequency channels in each spw, to provide imaging at 30 equally spaced frequencies ranging from 3.4 to 18 GHz, with center frequencies $f_{\text{GHz}} = 2.92 + n/2$, where n is the spw number from 1 to 30. The EOVSAs images in spws 1–26 for the three times marked in Figure 1 are shown in Figure 2 as filled 50% contours overlaid on AIA 193 Å images. The nominal full-width-half-max (FWHM) spatial resolution of these observations is elliptical, with major axis $113''7/f_{\text{GHz}}$ and minor axis $53''0/f_{\text{GHz}}$. During the CLEAN process, a circular restoring beam was used of FWHM $89''7/f_{\text{GHz}}$ for frequencies up to 14.9 GHz, while the size was fixed at $6''$ above 15 GHz. Thus, the frequency range of 3.4–18 GHz corresponds to a restored range of $25''7$ – $6''$.

2.1. EOVSAs Source Morphology

At time t_1 shown in Figures 2(a), (b), the EOVSAs source at lower frequencies is complex, consisting of a bright central source located well above the bright AIA loops, flanked by two more-distant sources associated with the legs of a much larger loop that appears to be associated with the coronal mass ejection. In addition, sources at the lowest few frequencies in Figure 2(b) appear distributed along a line connecting the AIA bright loops with a rapidly expanding, tear-drop-shaped cavity seen faintly in 193 Å. In the standard solar flare model, the cavity would be identified with a rising flux rope (Long et al. 2018) and the line connecting it to the lower, bright loops might be identified as a signature of the reconnecting current sheet (Warren et al. 2018), although to avoid over-interpretation we will refer to it as a “plasma sheet.” The emission at different frequencies in the bright central source, seen most clearly in Figure 2(a), shows a clear dispersion in height, with the highest-frequency source being lowest and most compact, but still lying well above the bright AIA loops. This also agrees

well with the standard solar flare model, in which the MW emission comes from the most recently closed loops that contain newly accelerated electrons. However, the emission appears to be more confined to the loop tops than would be expected in the simplest interpretation of the standard model (e.g., Aschwanden & Benz 1997). One way to account for the confinement is to invoke a high mirror ratio in the initially collapsing loops (e.g., Fletcher & Martens 1998; Karlický & Kosugi 2004), but it is likely that turbulence and wave-particle interactions also play a role in mediating the trapping. The dispersion in height with frequency mainly reflects the fall-off of coronal magnetic field strength with height, as discussed in Section 3.

At the peak time t_2 shown in Figures 2(c), (d), the EOVSAs sources grow much brighter, reaching a brightness temperature of $\sim 3.3 \times 10^9$ K at the highest frequencies. The weaker flank sources can no longer be seen, and an investigation of the time profiles of brightness of these sources shows that they intrinsically fade during the brightening of the central source, i.e., they do not merely become undetectable as a result of the $\sim 20:1$ dynamic range that can be achieved in the EOVSAs images. By time t_2 , the flux rope seen earlier in AIA has long-since left the field of view, but the strong energy release continues in the lower corona behind it. The height dispersion of EOVSAs source positions with frequency is similar to that at the earlier time, but the overall height of the sources evolves upward to remain well above the growing AIA bright loops. The source shape at the highest frequency evolves toward a loop-like shape but is asymmetric and slightly offset to the south.

The EOVSAs source remains similar in shape to that in Figures 2(c), (d) for 10s of minutes, slowly rising and growing weaker, but eventually it bifurcates and moves to the sides of the rising AIA bright loops, as shown at time t_3 in Figures 2(e), (f). By this time, a bright ray has developed in AIA 193 Å, which was studied in more detail by Warren et al. (2018) in conjunction with EUV spectral imaging data from the EUV Imaging Spectrometer (EIS; Culhane et al. 2007) aboard Hinode (Kosugi et al. 2007) and interpreted as a plasma sheet at a temperature of ~ 20 MK. The EOVSAs emission seems to avoid this location and shows interesting frequency structure, with the southern source being stronger at high frequencies while the northern source dominates at low frequencies. This likely reflects differences in both magnetic field structure and electron energy distributions on the two flanks.

2.2. RHESSI Source Morphology

Also shown in Figure 2 as open contours are the *RHESSI* HXR source locations, with red contours showing the lower-energy, thermal source and blue contours showing the higher-energy, nonthermal source. At each of the three times, the HXR thermal source is located within the bright AIA 193 Å loops. The response function of the AIA 193 Å band has a peak at ~ 18 MK dominated by the highly ionized iron line Fe XXIV (O’Dwyer et al. 2010). The close spatial association between the HXR thermal source and the bright (or high emission measure) AIA 193 Å loops suggest the presence of dense, super-hot (~ 20 MK) plasma there, which was confirmed by the analysis of EIS data by Warren et al. (2018). At the initial time t_1 , Figure 2(a), a compact nonthermal footpoint HXR source is seen at the limb, which coincides with a bright kernel of white-light emission seen in

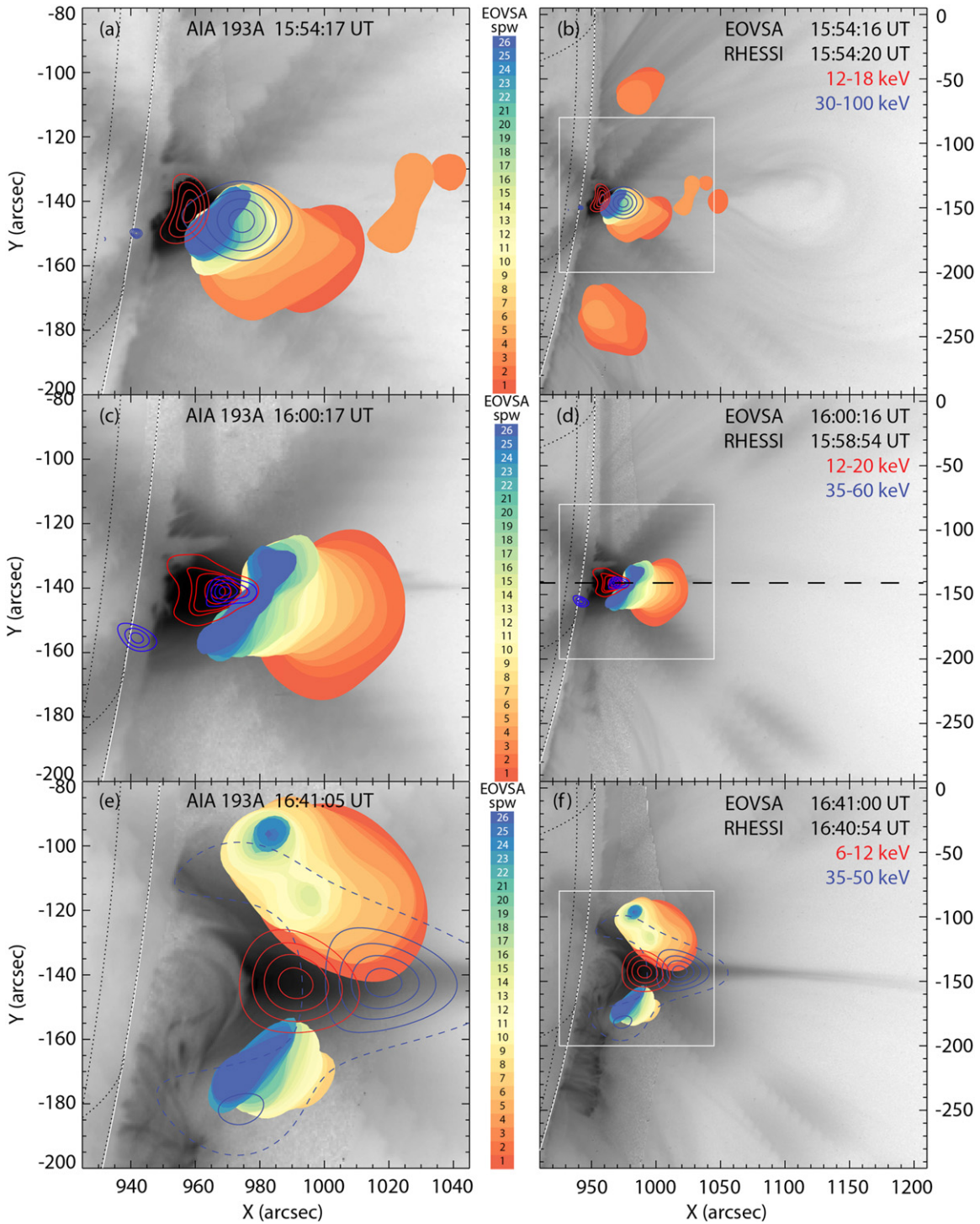


Figure 2. Comparison of AIA, *RHESSI*, and EOVSAs images at the three times marked in Figure 1. Each image shows the corresponding AIA 193 Å image (in reverse grayscale of log intensity) superposed with filled 50% contours of EOVSAs MW emission at 26 spectral windows, with hues shown in the color bar. *RHESSI* HXR 30%, 50%, 70%, and 90% contours are also superposed for two energy ranges. (a) Zoomed in (2×2 arcmin) field of view (FOV) of the limb flare near 15:54 UT. (b) Same as (a), but showing a larger 5×5 arcmin FOV. This view shows additional low-frequency MW sources flanking the main source to the north and south. The white box outlines the area shown in (a). (c) Same as (a), for the peak time near 16:00 UT, except *RHESSI* 12–20 keV contours are 40%, 55%, 60%, 75% and 90%. (d) 5×5 arcmin FOV corresponding to (c). The horizontal dashed line marks the position of the cut used for the height–time plots of Figures 3 and 4. (e) Same as (a), for a time near 16:41 UT in the decay phase. (f) 5×5 arcmin FOV corresponding to (e). The dashed contour in (e) and (f) is the 10% contour for the *RHESSI* 35–50 keV image.

continuum images from the Helioseismic and Magnetic Imager (Scherrer et al. 2012) at this time. The conjugate footpoint HXR source is presumably hidden beyond the limb. For similar events, see Krucker et al. (2015). A larger, more extended nonthermal HXR source is shown in Figure 2(a) at a

position that agrees well with the MW emission above the AIA bright loops. In order to image this weak nonthermal source, a two-step CLEAN procedure (Krucker et al. 2011) was used in which the brighter footpoint source was first imaged and subtracted from the HXR visibility data. A second

stage of CLEAN using the subtracted visibilities revealed the weaker source, which a series of imaging tests shows is quite robust.

At the peak time t_2 shown in Figures 2(c), (d), the *RHESSI* nonthermal 35–60 keV HXR source is found to be about $10''$ higher than the thermal 12–20 keV HXR source, but confined to the high-density region of the upper part of the AIA bright loops, at a projected height of ~ 25 Mm. Although *RHESSI* HXR data extend to still higher energies at this peak time, the high level of pulse pile-up means that imaging at higher energies requires further investigation, and therefore we do not show such higher-energy HXR images in Figures 2(c), (d).

After time t_2 , *RHESSI* entered the SAA and did not observe the Sun again until time t_3 shown in Figures 2(e), (f). By this time, the AIA bright loops have grown to much greater heights (~ 45 Mm), and the nonthermal HXR emission extends above the densest part of the 193 Å loops, encompassing the lower part of the bright ray and falling between the bifurcated MW sources. The 10% contour for the *RHESSI* nonthermal source is shown dashed, and indicates that the region of nonthermal HXR emission extends along the outside of the AIA bright loops, similar to the MW emission.

2.3. Temporal Development

To visualize the temporal development of AIA, EOVSAs, and *RHESSI* sources, we construct height–time stack plots in Figure 3, along a cut taken parallel to the heliocentric x axis at position $y = -141''$ bisecting the AIA loops. The position of the cut is shown by the black-dashed line in Figure 2(d). The time resolution of the AIA data is 12 s, while the time resolution of the EOVSAs is 4 s (i.e., we made the EOVSAs at one-quarter of the available resolution of 1 s). The initial rise of the ejecta and flux rope during the first 10 minutes, which were studied by Doschek et al. (2018) and Long et al. (2018), manifests as an upward-moving feature apparent in the AIA 193 Å and 131 Å data, outlined with black-dashed curves in Figures 3(a) and (b), respectively. The slower rise of the newly formed EUV “post-flare” loops occurs steadily throughout the period. The corresponding EOVSAs data for 5.42 and 13.42 GHz, shown in Figures 3(c) and (d), respectively, also show the same steady rise in height at least after about 15:56 UT when the lower-frequency emission associated with the plasma sheet has faded. Figures 3(e), (f) repeat the AIA data from the upper panels, now overlaid with EOVSAs contours from the middle panels to better demonstrate that the MW emission is located well above the EUV loops. In each panel, the height ranges of the *RHESSI* sources at the two times of Figures 2(a), (c) are shown by the vertical bars, with red representing the thermal (~ 12 keV) source and blue the nonthermal (~ 35 keV) source. The line labeled “Solar limb” in Figure 3(c) marks the approximate height of the EUV limb. The photosphere is $10''$ lower.

Figure 4(a) better shows the frequency dependence of source height, where the symbols are color-coded in frequency from red (spw 1 = 3.42 GHz) to blue (spw 30 = 17.92 GHz). The centroid source heights were determined by Gaussian fitting the one-dimensional profile of brightness temperature versus height for each frequency and time. The red symbols in Figure 4(a) show the tendency of the low-frequency EOVSAs sources to follow the bright ejecta up to about 15:51 UT, after which the fading emission from the ejecta causes the source centroid to move back to the rising post-flare loops. Then, from

15:52–15:55 UT, the low-frequency source extends upward again, along the plasma sheet below the rapidly rising flux rope. This can also be seen in the contours of the 5.42 GHz source in Figure 3(e). After 15:55 UT, the MW emission at all frequencies settles into a slow increase in height with time, maintaining a dispersion of height with frequency. The black curve in Figure 4(b) shows the median height of the source in the frequency range 15.92–17.92 GHz, located near the top of the brightest EUV emission. Remarkably, this source height closely tracks the AIA 193 Å intensity contour. The speed at the time of the most rapid rise, from 15:58:24 to 16:01:44 UT is ~ 30 km s $^{-1}$. The more rapid rise in EUV indicated by the yellow dashed curve in Figure 4(b) is due to previously mentioned bright ray propagating outward at ~ 288 km s $^{-1}$ along the plasma sheet, according to Warren et al. (2018).

3. Spectral Diagnostics

The EOVSAs multi-frequency images form a four-dimensional data cube, two spatial, one spectral, and one temporal. Prior to the completion of EOVSAs, Gary et al. (2013) performed a quantitative simulation of a flaring loop and explored the diagnostic power of the technique of MW imaging spectroscopy. Now, for the first time, we have actual EOVSAs data that permit the type of quantitative analysis simulated there. The approach is to obtain brightness temperature spectra over the frequency axis along different lines of sight in space, and then do a multi-parameter fit (Fleishman et al. 2009) assuming that the source is homogeneous along the line of sight. A full analysis of the data in this manner is beyond the scope of this work and will be published elsewhere. Here, we illustrate the procedure for four lines of sight at 15:54 UT, the time of the images shown in Figures 2(a), (b). Figure 5 shows the result, presented in the same format as in the Gary et al. (2013) paper, for comparison. We emphasize that these results are preliminary pending further refinement of the absolute flux calibration, which is now underway.

The same EOVSAs data shown in Figure 2(b) are used to create a “true-color” image in Figure 5(f), where images at 28 frequencies are apportioned different red–green–blue weights according to their frequency. EOVSAs single-frequency images within the white box are shown in Figure 5(a). The EOVSAs source shape changes with frequency from a cusp-shaped source at mid-frequencies (e.g., the 7.9 GHz image in Figure 5(a)) evolving toward a more loop-like shape at higher frequencies (15.9 GHz image). These position and morphology changes with frequency correspond to position-dependent spectral shapes. The spectra at the four locations indicated in Figure 5(f) are shown by the symbols in Figures 5(b)–(e). The displayed spectra are scaled from the original brightness temperature units to solar flux units (sfu/pxel, where 1 sfu = 10^{-22} W m $^{-2}$ Hz $^{-1}$, and each map pixel has an area of $2'' \times 2''$). The $\pm 1\sigma$ errors shown are based on residual fluctuations in a region of the maps away from any sources. The relatively large error bars on the high-frequency spectral points for points 3 and 4 in Figures 5(d), (e) reflect the fact that they come from low-brightness regions in the same map as the very bright source centered at point 1, demonstrating that the dynamic range of these images is about 20:1.

As shown in Figure 5(f), the points 1–3 are located at different heights along the bisector of the EUV loops, while point 4 is at the same coronal height as point 1 but to the south edge of the source. The spectra in Figures 5(b)–(d) show that

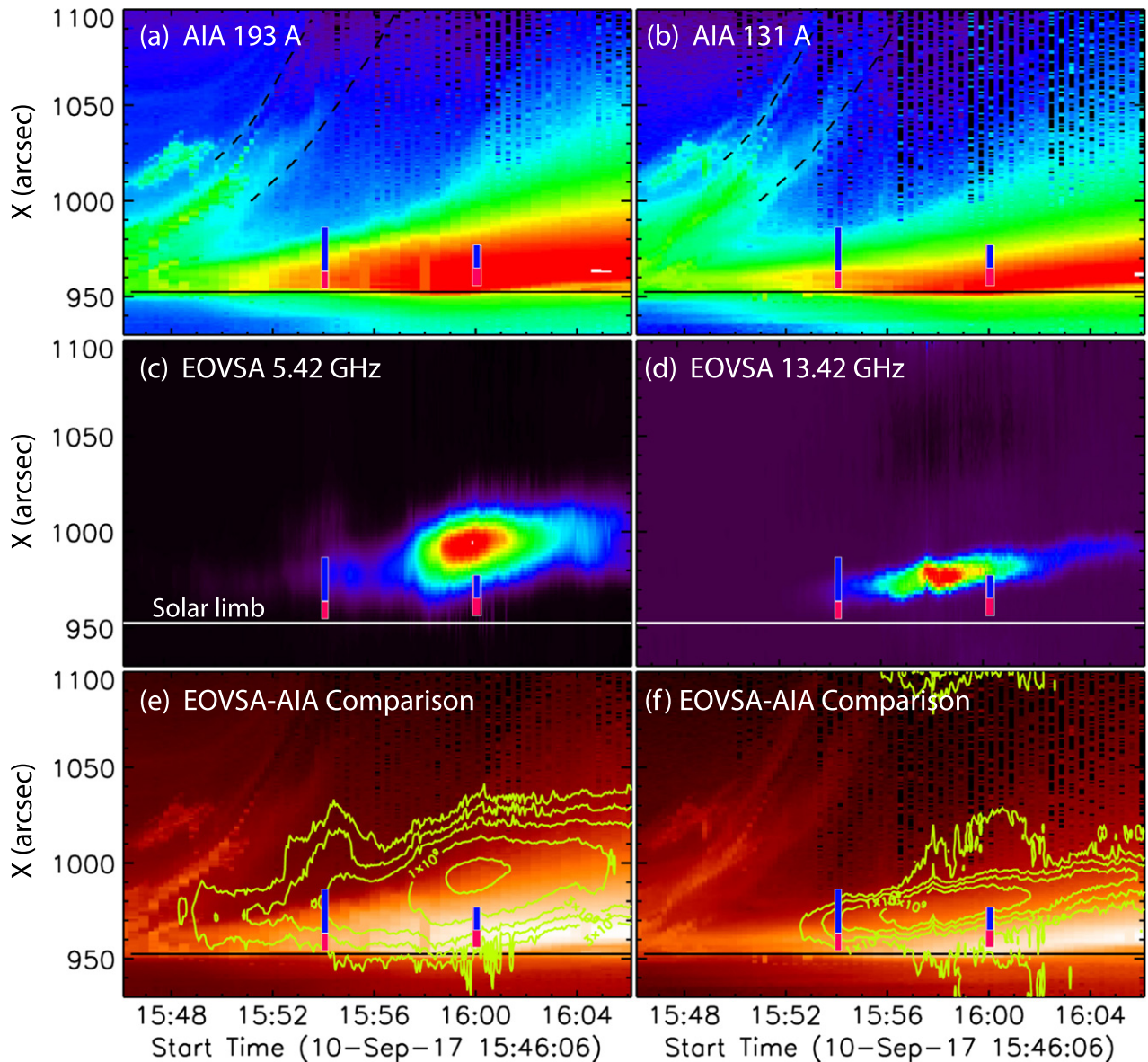


Figure 3. Height–time stack plots of AIA, EOVSAs, and *RHESSI* data from a horizontal cut at vertical position $y = -141''$ in Figure 2. The red vertical bars in each panel show the 50% contour height range of the *RHESSI* thermal sources at times t_1 and t_2 , from Figures 2(a), (c), while the blue bars show the corresponding height range of the *RHESSI* nonthermal sources. The time range covers 20 minutes, from 15:46 to 16:06 UT. (a) AIA 193 Å intensity, log-scaled. The black-dashed curves schematically show the leading and trailing edges of the flux rope. (b) AIA 131 Å intensity, log-scaled. (c) EOVSAs 5.42 GHz brightness temperature, linearly scaled. (d) EOVSAs 13.42 GHz brightness temperature, linearly scaled. (e) The same AIA 193 Å intensity as in (a) overlaid with the 5.42 GHz brightness temperature contours at 30, 100, 300, 1000, and 3000 MK. (f) The AIA 131 Å intensity as in (b), overlaid with the 13.42 GHz brightness temperature contours at 100, 300, 1000, and 3000 MK.

the peak frequency moves progressively to lower frequencies as the height increases, as would be expected for a decreasing magnetic field strength with height. The spectrum at point 4 is similar to point 3 but seems to be flatter at high frequencies. Using the homogeneous source multi-parameter fitting procedure for gyrosynchrotron emission from an isotropic power-law distribution of electrons, described by Fleishman et al. (2009), we obtain the red curves, which are acceptable fits to the data points (reduced χ^2 ranges from 0.2 to 0.5, which suggests that the error bars in Figures 5(b)–(d) may in fact over-estimate the variance in the data). The two key parameters, the magnetic field strength B and the power-law index of the electron energy distribution, δ , are listed as text in each spectrum panel. As expected from the shift of the spectral peak with height in the

corona, the derived magnetic field strength drops from 520 G at point 1 to 148 G at point 3. It is interesting, however, that the magnetic field strength at point 4, which is at the same height as point 1, is the same as at point 1, even though the spectral peak frequency is closer to that at point 3. The uncertainties in B from the fitting procedure are relatively small, ranging from 10% to 15%, but quantifying the systematic uncertainties requires modeling. The power-law index is around $\delta = 2.7$ at points 1 and 2, and steepens to $\delta = 5.6$ at point 3, while the spectrum is extremely flat at point 4 with $\delta = 1.86$. Again, the fitting uncertainties in δ are small, around 5%, but systematic uncertainties remain to be quantified.

It is useful to compare these derived parameters with spectral diagnostics from the *RHESSI* HXR data taken around

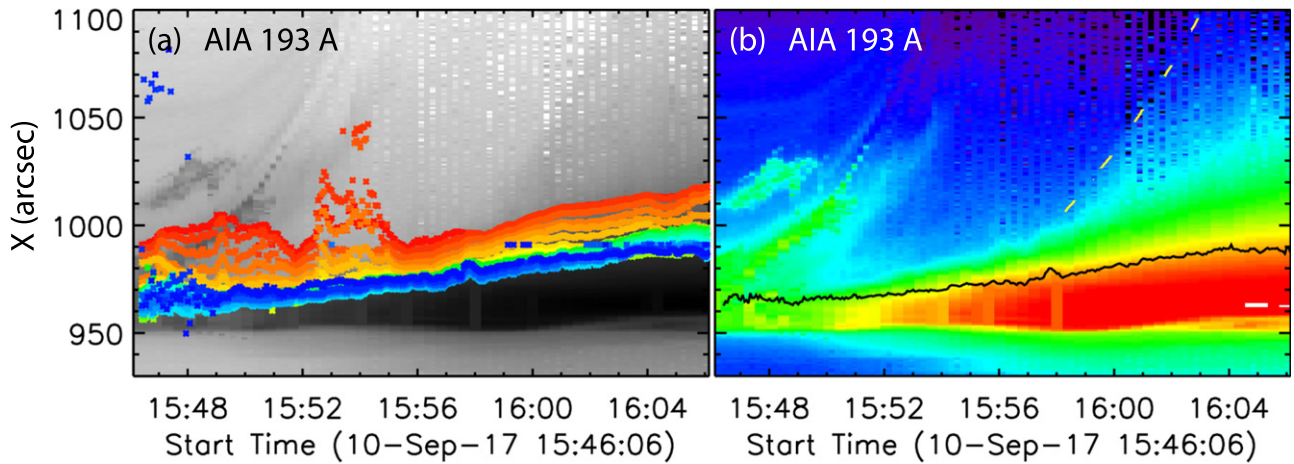


Figure 4. (a) Height–time stackplot of AIA 193 Å log-scaled in reverse grayscale (brightest emission is black), with EOVSA centroid source heights at all 30 frequencies, shown as symbols color-coded in frequency from red (spw 1 = 3.42 GHz) to blue (spw 30 = 17.92 GHz). (b) Repeat of log-scaled AIA 193 Å height–time plot in rainbow colors, overplotted with the median centroid height (black curve) of EOVSA spw 26–30 (15.92–17.92 GHz). The yellow dashed curve indicates the leading edge of the bright ray that grows rapidly along the plasma sheet.

15:54 UT. Figure 6 shows the results of such spectral analysis assuming a thermal-plus-single-power-law photon spectrum. The flare-integrated HXR photon spectrum is shown by the black curve, which sums the contributions from the looptop thermal source, the compact footpoint source near the limb seen in Figure 2(a), and the extended above-the-looptop nonthermal source. For comparison with EOVSA, we are interested in this latter source, which is co-spatial with the EOVSA source region, but the HXR emission is too weak for accurate imaging spectroscopy. However, the compact source is suitable for such imaging spectroscopy, which yields the blue crosses in Figure 6 and can be fit with a photon power-law index $\gamma = 3.4$ as shown by the blue line. We then use the imaging spectroscopy result of the footpoint as a fixed input to the spatially integrated spectral fitting, together with two free fit functions, a thermal component and a second power-law that represents the nonthermal coronal source. The fit to the nonthermal coronal source is shown in purple with a power-law index of $\gamma \approx 4.4 \pm 0.1$. For the comparison with the radio derived spectral indices, we need the spectral index of the instantaneous distribution of nonthermal electrons, which comes from the thin-target model; thus, we get $\delta_{\text{HXR}} = \gamma - 0.5 \approx 3.9$. The brightness center of the coronal HXR source is between points 2 and 3 in Figure 5(f); thus, having $\delta_{\text{HXR}} = 3.9$ in between $\delta_2 = 2.7$ and $\delta_3 = 5.6$ derived from EOVSA looks reasonable.

4. Discussion

The combination of EUV, HXR, and MW imaging of the central source during the early impulsive phase (15:54 UT) matches expectations from the CSHKP model very well. The bright EUV-emitting loops overlap the *RHESSI* thermal component, while the *RHESSI* nonthermal component comes from an extended region above them. The EOVSA emission overlaps the *RHESSI* nonthermal source but extends to greater heights at the lower MW frequencies where the magnetic field strength is lower. We have shown for the first time that it is possible to fit gyrosynchrotron spectra to spatially resolved MW observations and derive a reliable set of physical parameters as a function of time and space. Spectral diagnostics of the accelerated electron spectrum derived from HXR and MW observations are broadly

consistent. A more detailed study is underway to exploit this technique to create dynamic parameters maps of the entire emitting region, as simulated by Gary et al. (2013).

After the initial impulsive phase of the event, the closed-field region below the plasma sheet becomes the dominant region of MW emission, in agreement with the CSHKP model. We expect that the bright and growing MW emission during this time is due to the continued creation of new loops combined with efficient electron trapping, which enables an increasing accumulation of high-energy electrons as the acceleration continues. Enhanced trapping due to an initially high mirror ratio (e.g., Karlický & Kosugi 2004) may explain the confinement of the MW sources to the loop tops. For a static source, Coulomb collisions should lead to preferential loss of lower-energy particles, which would lead to progressive hardening and a positive delay of the MW peak with respect to frequency, which is opposite to the sense of delay shown in Figures 1(a), (b). However, in this event the source is not static but growing upward as new loops are formed, which provides an opportunity for a more complex temporal evolution. The inferred energy of these MW-emitting electrons is extremely high. The peak brightness temperature T_b exceeds 3×10^9 K, which corresponds to a bulk electron energy for the emitting particles of $E > T_{\text{eff}}/k \approx 270$ keV, where $T_{\text{eff}} \approx T_b$ (cf. Dulk 1985) is the effective electron temperature assuming optically thick emission, and k is the Boltzmann constant. The relatively flat energy distribution ($\delta = 2.7$) implies the presence of >1 MeV electrons in significant numbers in the region, although quantitative estimates require additional analysis.

Energy release and acceleration of particles to high energies continues for hours after the event began, as revealed by EOVSA and by the continued level of >100 MeV emission detected by *Fermi* (Omodei et al. 2018). The EOVSA source becomes distinct from the HXR source during this time ($\sim 16:41$ UT). Both thermal and nonthermal *RHESSI* images match well the denser, EUV-emitting regions while the EOVSA source bifurcates and avoids the dense regions. Whether this is primarily due to suppression of the MW emission or a relative lack of higher-energy electrons in the denser regions remains to be determined by the more-thorough spectral analysis now underway.

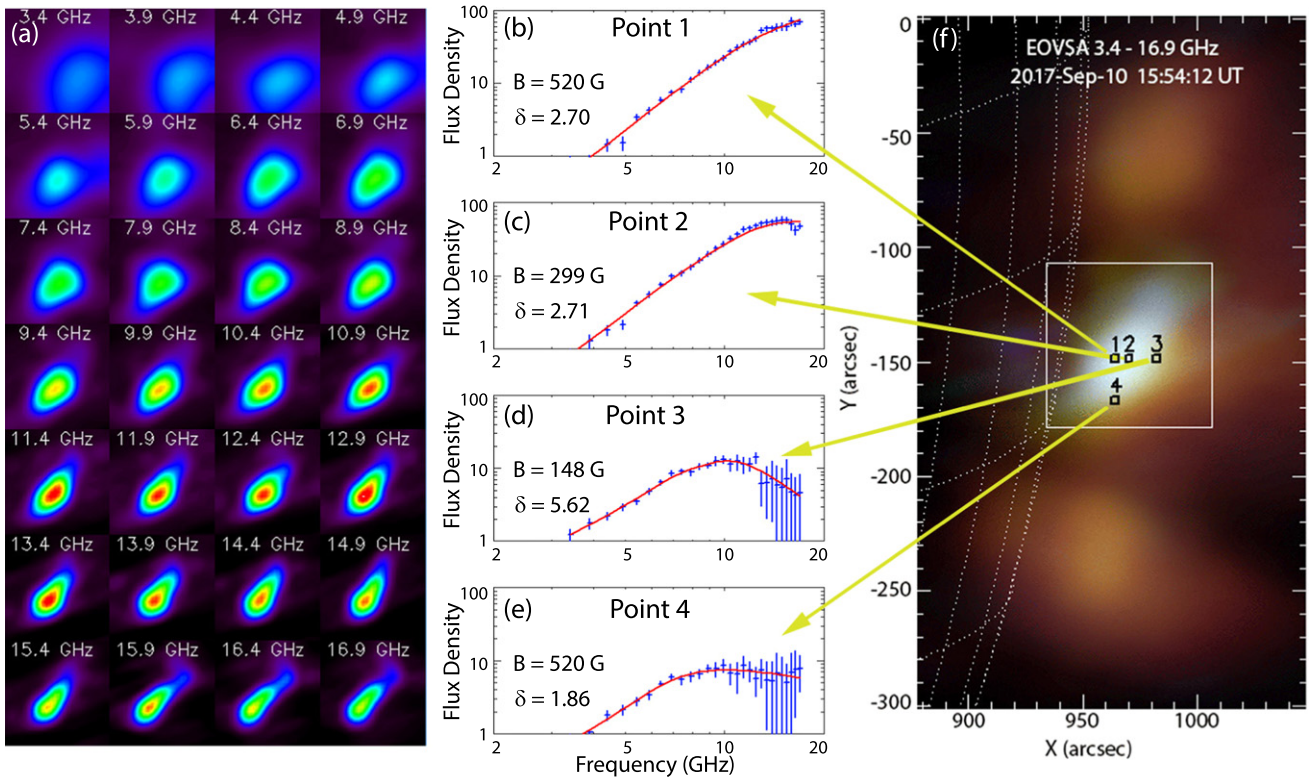


Figure 5. The same analysis as for the simulations in Gary et al. (2013) but with data from the time shown in Figures 2(a), (b). (a) Individual images at 28 frequencies, from the location of the white box in the overview image in panel (f). (b)–(e) Measured flux-density spectra (points with $\pm 1\sigma$ error bars) in single pixels of the images in panel (a), corresponding to locations 1–4 marked in panel (f), and corresponding multi-parameter fits (red lines). (f) A “true-color” representation of the EOVSA data cube, combining images at the 28 frequencies shown in panel (a).

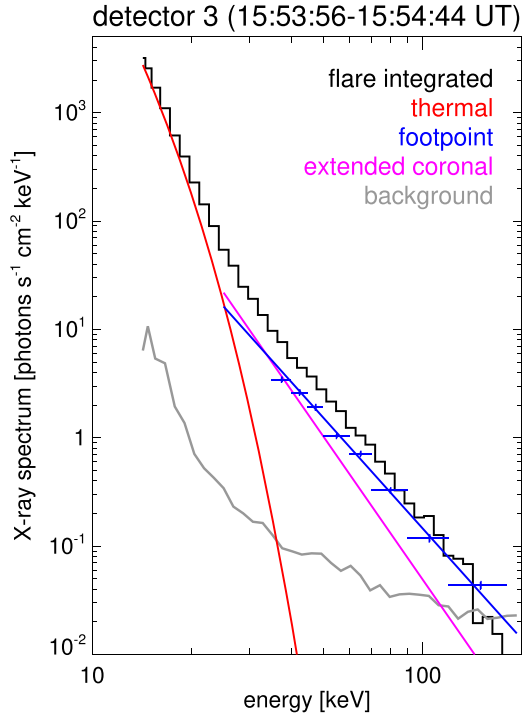



Figure 6. *RHESSI* photon spectrum, where the black curve is the integrated spectrum, the red curve is the thermal source spectrum, and the blue points with a power-law fit are the energy distribution from the compact footpoint source. After subtraction, the implied spectrum of the extended coronal source at higher energies is shown as the purple line. The power-law index of the compact source is $\gamma = 3.4$ while that of the extended source is $\gamma = 4.4$.

5. Conclusion

We have used our coverage of the well-observed X8.2 limb flare, SOL2017-09-10, as an opportunity to present the first science results from a new, multi-frequency imaging array, the EOVSA. The results both agree with the standard CSHKP model for solar flares and suggest the need for amending it, by revealing new details of the spatial distribution of high-energy electrons. MW observations at high, optically thin frequencies provide source information in regions of high magnetic field strength, which are limited to relatively small, closed magnetic loops formed below the reconnection region. The EOVSA images at lower MW frequencies early in the event reveal the prompt presence of high-energy electrons over a much larger region, including the plasma sheet extending between the lower, newly formed loops and the rising flux rope, and the legs of a much larger loop well outside the traditionally observed, reconnected loops. Although isolated examples of such large source regions have been reported in the literature, as noted in Section 1, the ability of EOVSA to simultaneously image the whole MW spectrum, including both high- and low-frequency emission, has provided a panoramic view of the entire system of energetic electrons. Revealing the large spatial extent of the region of high-energy electrons is one of the key new insights provided by EOVSA, but equally important is its ability to provide quantitative diagnostics of plasma and particle parameters through MW imaging spectroscopy. Further analysis of the dynamically evolving, spatially resolved spectra is underway.

We thank the many talented engineers and technicians who worked to make EOVSa a reality, in particular our site manager Kjell Nelin. This work was supported by NSF grants AST-1615807, AST-1735405, AGS-1654382, AGS-1723436, AGS-1817277 and NASA grants NNX14AK66G, 80NSSC18K0015, NNX17AB82G, NNX16AL67G, and 80NSSC18K0667 to New Jersey Institute of Technology. The *RHESSI* related part of this work is supported by NASA contract NAS 5-98033. S. W. acknowledges support from AFOSR LRIRs 14RV14COR and 17RVCOR416.

ORCID iDs

Dale E. Gary  <https://orcid.org/0000-0003-2520-8396>
 Bin Chen  <https://orcid.org/0000-0002-0660-3350>
 Brian R. Dennis  <https://orcid.org/0000-0001-8585-2349>
 Gregory D. Fleishman  <https://orcid.org/0000-0001-5557-2100>
 James M. McTiernan  <https://orcid.org/0000-0002-3038-176X>
 Gelu M. Nita  <https://orcid.org/0000-0003-2846-2453>
 Stephen M. White  <https://orcid.org/0000-0002-8574-8629>
 Sijie Yu  <https://orcid.org/0000-0003-2872-2614>

References

- Aschwanden, M. J., & Benz, A. O. 1997, *ApJ*, **480**, 825
 Atwood, W. B., Abdo, A. A., Ackermann, M., et al. 2009, *ApJ*, **697**, 1071
 Bastian, T. S., & Gary, D. E. 2005, in ASP Conf. Ser. 345, From Clark Lake to the Long Wavelength Array: Bill Erickson's Radio Science, ed. N. Kassim et al. (San Francisco, CA: ASP), 142
 Carmichael, H. 1964, *NASSP*, **50**, 451
 Culhane, J. L., Harra, L. K., James, A. M., et al. 2007, *SoPh*, **243**, 19
 Dennis, B. R. 1988, *SoPh*, **118**, 49
 Doschek, G. A., Warren, H. P., Harra, L. K., et al. 2018, *ApJ*, **853**, 178
 Dulk, G. A. 1985, *ARA&A*, **23**, 169
 Fleishman, G. D., Nita, G. M., & Gary, D. E. 2009, *ApJL*, **698**, L183
 Fleishman, G. D., Nita, G. M., & Gary, D. E. 2015, *ApJ*, **802**, 122
 Fleishman, G. D., Nita, G. M., & Gary, D. E. 2017, *ApJ*, **845**, 135
 Fletcher, L., & Martens, P. C. H. 1998, *ApJ*, **505**, 418
 Gary, D. E., & Keller, C. U. (ed.) 2004, *Solar and Space Weather Radiophysics—Current Status and Future Developments* (Berlin: Springer)
 Gary, D. E., Chen, B., Grammer, W., et al. 2018, *SoPh*, submitted
 Gary, D. E., Fleishman, G. D., & Nita, G. M. 2013, *SoPh*, **288**, 549
 Gary, D. E., & Hurford, G. J. 1989, *ApJ*, **339**, 1115
 Guidice, D. A., & Castelli, J. P. 1975, *SoPh*, **44**, 155
 Hanaoka, Y. 1997, *SoPh*, **173**, 319
 Hirayama, T. 1974, *SoPh*, **34**, 323
 Karlický, M., & Kosugi, T. 2004, *A&A*, **419**, 1159
 Kopp, R. A., & Pneuman, G. W. 1976, *SoPh*, **50**, 85
 Kosugi, T., Matsuzaki, K., Sakao, T., et al. 2007, *SoPh*, **243**, 3
 Krucker, S., Kontar, E. P., Christe, S., Glesener, L., & Lin, R. P. 2011, *ApJ*, **742**, 82
 Krucker, S., & Lin, R. P. 2008, *ApJ*, **673**, 1181
 Krucker, S., Saint-Hilaire, P., Hudson, H. S., et al. 2015, *ApJ*, **802**, 19
 Kucera, T. A., Dulk, G. A., Gary, D. E., & Bastian, T. S. 1994, *ApJ*, **433**, 875
 Kuroda, N., Gary, D. E., Wang, H., et al. 2018, *ApJ*, **852**, 32
 Lee, J. W., Gary, D. E., & Zirin, H. 1994, *SoPh*, **152**, 409
 Lemen, J. R., Title, A. M., Akin, D. J., et al. 2012, *SoPh*, **275**, 17
 Li, Y., Xue, J. C., Ding, M. D., et al. 2018, *ApJL*, **853**, L15
 Lin, R. P., Dennis, B. R., Hurford, G. J., et al. 2002, *SoPh*, **210**, 3
 Long, D. M., Harra, L. K., Matthews, S. A., et al. 2018, *ApJ*, **855**, 74
 Masuda, S., Kosugi, T., Hara, H., Tsuneta, S., & Ogawara, Y. 1994, *Natur*, **371**, 495
 Meegan, C., Lichti, G., Bhat, P. N., et al. 2009, *ApJ*, **702**, 791
 Melnikov, V. F., Shibasaki, K., & Reznikova, V. E. 2002, *ApJL*, **580**, L185
 Nakajima, H., Nishio, M., Enome, S., et al. 1994, *IEEEP*, **82**, 705
 Nishio, M., Yaji, K., Kosugi, T., Nakajima, H., & Sakurai, T. 1997, *ApJ*, **489**, 976
 Nita, G. M., Gary, D. E., & Lee, J. 2004, *ApJ*, **605**, 528
 Nita, G. M., Hickish, J., MacMahon, D., & Gary, D. E. 2016, *JAI*, **5**, 1641009
 O'Dwyer, B., Del Zanna, G., Mason, H. E., Weber, M. A., & Tripathi, D. 2010, *A&A*, **521**, A21
 Omodei, N., Pesce-Rollins, M., Longo, F., Allafort, A., & Krucker, S. 2018, arXiv:1803.07654
 Scherrer, P. H., Schou, J., Bush, R. I., et al. 2012, *SoPh*, **275**, 207
 Schmahl, E. J., Schmelz, J. T., Saba, J. L. R., Strong, K. T., & Kundu, M. R. 1990, *ApJ*, **358**, 654
 Sturrock, P. A. 1966, *Natur*, **211**, 695
 Wang, H., Gary, D. E., Lim, J., & Schwartz, R. A. 1994, *ApJ*, **433**, 379
 Wang, H., Liu, C., Ahn, K., et al. 2017, *NatAs*, **1**, 0085
 Warren, H. P., Brooks, D. H., Ugarte-Urra, I., et al. 2018, *ApJ*, **854**, 122
 Yan, X. L., Yang, L. H., Xue, Z. K., et al. 2018, *ApJL*, **853**, L18